

# Plasma Molding Over Surface Topography: Simulation and Measurement of Ion Fluxes, Energies and Angular Distributions Over Trenches in RF High Density Plasmas

Doosik Kim, Demetre J. Economou, J. R. Woodworth, P. A. Miller, R. J. Shul, B. P. Aragon, T. W. Hamilton, and C. G. Willison

**Abstract**—A two-dimensional (2-D) fluid/Monte Carlo (MC) simulation model was developed to study plasma “molding” over a trench. The radio frequency sheath potential evolution and ion density and flux profiles over the surface were predicted with a self-consistent fluid simulation. The trajectories of ions and energetic neutrals (resulting by ion neutralization on surfaces or charge exchange collisions in the gas phase) were then followed with a MC simulation. For sheath thickness  $L_{sh}$  comparable to the trench width  $D$ , ions were strongly deflected toward the trench sidewall, and the ion flux along the trench surface contour was highly nonuniform. Irrespective of the trench depth, the normalized spatially-average ion flux at the trench mouth showed a minimum at  $L_{sh}/D \sim 1.0$ . The normalized spatially-average ion flux at the trench bottom decreased with increasing trench depth (or aspect ratio). As the trench sidewall was approached, the energy spread  $\Delta E$  of the ion energy distributions (IEDs) at the trench bottom decreased for a thin sheath, but increased for a thick sheath. At the trench bottom, the neutral flux was comparable to the ion flux over the entire range of sheath thickness studied. Simulation results were in good agreement with experimental data on ion flux, IEDs, and ion angular distributions at the trench bottom.

**Index Terms**—Ion angular distribution, ion energy distribution (IED), ion flow in trenches, Monte Carlo (MC) simulation, plasma molding, two-dimensional (2-D) plasma sheath.

## I. INTRODUCTION

A SHEATH forms over any wall in contact with plasma. The sheath confines electrons in the plasma such that the net current escaping the plasma is zero. The sheath normally contains a net positive charge and is a region of relatively high electric field, pointing toward the confining wall. Therefore, positive

ions accelerate in the sheath and strike the wall with high energies (depending on the sheath voltage) [1]. The sheath over a homogeneous infinite planar surface is correspondingly planar [one-dimensional (1-D)]. However, when the surface contains geometrical features with sizes on the order of or larger than the sheath thickness, the sheath will try to wrap around the contour of the features. This is called *plasma molding*.

The important length scales that control the behavior of the sheath are the plasma sheath thickness,  $L_{sh}$ , and the size of surface features. As an example, Fig. 1 provides a schematic of plasma molding over a trench of width  $D$ . In case (a),  $L_{sh} \ll D$ , the sheath thickness is much smaller than the trench width. The plasma-sheath interface (meniscus) conforms to the shape of the surface topography. At the other extreme (case c),  $L_{sh} \gg D$ , the plasma-sheath interface is essentially planar, as if the trench were nonexistent. The plasma simply does not feel the presence of the surface topography. This situation is encountered in microelectronics, where the feature size is below a micron while the sheath is at least hundreds of microns thick. In the intermediate case (b),  $L_{sh} \sim D$ , the plasma-sheath meniscus “bends” gently over the trench mouth becoming planar away from the feature. This situation may be encountered in microelectromechanical systems (MEMS) fabrication [2]. The depth of the trench  $H$  (or aspect ratio  $\equiv H/D$ ) is another important parameter, which affects ion flow inside the trench. Cases (a)–(c) would result in drastically different flux, energy, and angular distributions of ions impacting along the surface contour. Fig. 1 depicts the case of a dc (time-invariant) sheath. In case of radio frequency (RF) biased surfaces, the sheath thickness will be a function of time. It should be noted that, even in the case of very thick sheath (case c), the sheath structure will still be two-dimensional (2-D) near the surface topography (over a distance extending several times  $D$  from the surface) [3].

Etching or deposition of thin films on substrates containing surface topography (trenches, holes, etc.), are crucial operations in microelectronics manufacturing and the fabrication of MEMS [2]. The reaction rate along the surface contour depends on the ion flux, energy, and angular distributions. These, in turn, depend on plasma molding over the features. In Fig. 1(c), for example, ions will be mainly perpendicular to the trench bottom, as they approach the feature. Ions may suffer some

Manuscript received November 8, 2002; revised February 21, 2003. This work was supported by Sandia National Laboratories, the National Science Foundation (CTS-0072854), the National Institute of Standards and Technology, and the Institute of Space Systems Operations (ISSO) of the University of Houston. Sandia is a multiprogram laboratory operated by Sandia Corporation, a Lockheed Martin Company, for the United States Department of Energy under Contract DE-ACO4-94AL85000.

D. Kim and D. J. Economou are with the Plasma Processing Laboratory, Department of Chemical Engineering, University of Houston, Houston, TX 77204-4004 USA (e-mail: economou@uh.edu).

J. R. Woodworth, P. A. Miller, R. J. Shul, B. P. Aragon, and T. W. Hamilton are with the Sandia National Laboratories, Albuquerque, NM 87185-1193 USA.

C. G. Willison is with the L & M Technologies, Albuquerque, NM 87109-5802 USA.

Digital Object Identifier 10.1109/TPS.2003.815248

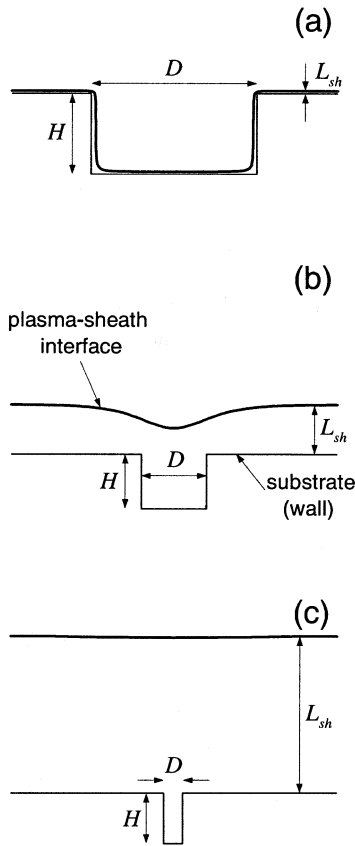


Fig. 1. Plasma molding over a trench. The width and depth of the trench are  $D$  and  $H$ , respectively. When the sheath thickness  $L_{sh}$  is much smaller than  $D$  [case (a)], the plasma-sheath interface conforms almost exactly to the surface topography. In the other extreme ( $L_{sh} \gg D$ ), the plasma-sheath interface is essentially planar. Case (b) ( $L_{sh} \sim D$ ) is an intermediate situation between the two limiting cases.

decollimation near the feature mouth, however, which can lead to artifacts etched into the features [3], [4]. Such artifacts seem to depend on whether the surface is conductive or insulating, as well as plasma reactor operating conditions (pressure, bias frequency, etc.). In Fig. 1(b), however, ions may strike the trench bottom with substantial angles off normal [5], [6]. Besides MEMS fabrication, plasma molding finds application in ion extraction through grids (ion beams, plasma thrusters) [7], plasma immersion ion implantation [8], and neutral beam sources [9].

The literature on 1-D sheaths is extensive [10]–[20]. An array of issues have been addressed over the years including dc and RF potential distribution, the Bohm criterion, ion energy and angular distributions, and the joining of the sheath to the bulk plasma. In contrast, sheath formation and potential distribution over geometrical features have not been adequately addressed in the literature. A few authors presented 2-D numerical simulation of ion extraction relevant to plasma immersion ion implantation (PIII) [21]–[23]. Numerical results reported so far, although useful, are limited to PIII and are not applicable to 2-D RF biased sheaths of relatively low voltages (10–100s of V). Other authors [24], [25] have solved for the potential distribution in a matrix sheath (spatially uniform ion density) over 2-D topographical features neglecting ion motion. In these studies, the ion flux, ion energy distributions (IEDs), and ion angular

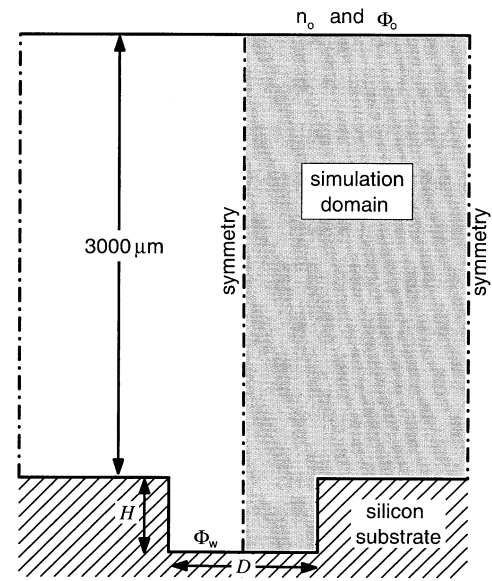


Fig. 2. Domain and boundary conditions used in the simulation. A 2-D trench is located in a conducting silicon substrate. Half of the domain (between two symmetry planes) was simulated. The plasma density  $n_0$  was specified at the upper boundary. The electric potential was specified at the upper boundary ( $\Phi_0$ ) and on the silicon wall ( $\Phi_w$ ). Monte Carlo kinetic data were collected at the bottom of the trench.

distributions (IADs) along the surface contour were not determined.

In this paper, a 2-D fluid/Monte Carlo (MC) simulation is reported, in an effort to predict the ion flux, IEDs, and IADs along the surface of a 2-D trench, in contact with a RF high density Ar plasma. Energetic (fast) neutrals resulting by neutralization of ions on the wall or by charge exchange collisions in the gas were also studied. A description of the model and numerical procedures are presented in Section II. The experimental apparatus used to measure ion fluxes, IEDs and IADs is described in Section III. Simulation results and comparison with experimental measurements are discussed in Section IV. Conclusions are drawn in Section V.

## II. SIMULATION

A schematic of the 2-D ( $x, y$ ) system studied is shown in Fig. 2. Away from the trench the sheath is 1-D and the literature on 1-D sheaths can be applied. The goal is to study the ion flux, IEDs and IADs as a function of position along the contour of the 2-D trench. For this purpose, a combined fluid/MC simulation was employed. The fluid simulation provided the 2-D RF electric field profiles. These were used as input to the (decoupled) MC simulation to follow ion (and fast neutral) trajectories through the sheath and onto the wall.

### A. Fluid Simulation

An electropositive plasma with one species of positive ion and electrons was considered. The governing equations are the 2-D compressible fluid equations (species and momentum balance) for ions, coupled with Poisson's equation for the electric potential [1], [26]. The Boltzmann relation was used for the electron density, assuming that the pressure force is balanced by the local electric field force with a neglect of electron inertia

TABLE I  
BASE VALUES OF PARAMETERS USED FOR SIMULATION

Electron temperature, $T_e$	3.7 eV
Potential at top boundary, $\Phi_o$	33 +17sin( $\omega_{rf}t$ ) V
Potential at substrate, $\Phi_w$	0 V (grounded)
Ion temperature (used for MC simulation)	0.1 eV
Transverse ion temperature (used for MC)	0.1 eV
Gas temperature	0.05 eV
Gas pressure	5 mTorr
rf frequency, $f_{rf}$ ( $=\omega_{rf}/2\pi$ )	13.56 MHz

[1]. It was further assumed that the ion distribution function is a drifting Maxwellian. Isothermal equations of state were used for both electrons and ions. The background neutral gas pressure and temperature (hence, density) were taken to be constant throughout.

The ion mass and momentum balance equations read

$$\frac{\partial n_i}{\partial t} + \nabla \circ (n_i \vec{u}) = 0 \quad (1)$$

$$\frac{\partial}{\partial t} (n_i \vec{u}) + \nabla \circ (n_i \vec{u} \vec{u}) = - \frac{en_i}{m_i} \nabla \Phi - \nu_m n_i \vec{u} \quad (2)$$

where  $n_i$ ,  $m_i$ , and  $\vec{u}$  are the ion density, ion mass, and ion–fluid velocity, respectively.  $\Phi$  is the electric potential and  $e$  is the elementary charge. Ions could suffer either elastic or charge exchange collisions with the background gas. Neither of these processes alters the ion density (no source or sink terms in the ion mass balance). However, these collisions affect the ion momentum as shown by the last term in (2), where  $\nu_m$  is the total collision frequency for momentum loss. Since a drifting Maxwellian is isotropic in the frame moving with the ion drift velocity, a viscous stress term was not included in the momentum equation [26]. The ion pressure force was ignored because the ion temperature is much lower than the electron temperature (cold ions). However, ion thermal effects were accounted for in the MC simulations (see Section II-B).

Poisson's equation with the Boltzmann relation for electrons reads

$$\nabla^2 \Phi = - \frac{e}{\epsilon_o} \left( n_i - n_o \exp \left( \frac{\Phi - \Phi_o}{T_e} \right) \right) \quad (3)$$

where  $\epsilon_o$  is the permittivity of free space,  $T_e$  is the electron temperature (in V), and  $\Phi_o$  and  $n_o$  are the values for electric potential and ion density, respectively, at the upper boundary (see Fig. 2). Parameter values are shown in Table I.

Fig. 2 also shows the computational domain and boundary conditions employed in this work. A highly conductive (equipotential) silicon (Si) substrate was located at the bottom of the domain. The electric potential was specified at the upper boundary ( $\Phi_o$ ) and on the equipotential (assumed grounded) substrate ( $\Phi_w$ ). A symmetry condition ( $\nabla_n \Phi = 0$ ) was applied at the side boundaries. The domain height (3000  $\mu\text{m}$  in Fig. 2), was always much thicker than the sheath thickness (Table II). Hence, the quasi-neutrality condition ( $n_i = n_e = n_o$ ) was applied at

TABLE II  
SELECTED SIMULATION CASES FOR 500- $\mu\text{m}$ -WIDE AND 500- $\mu\text{m}$ -DEEP TRENCHES. ONLY THE ION DENSITY AT THE UPPER BOUNDARY (FIG. 2) WAS VARIED, WHILE OTHER SIMULATION PARAMETERS WERE FIXED AS SHOWN IN TABLE I. THE RESULTING SHEATH THICKNESS AND ITS RATIO TO THE TRENCH WIDTH ARE ALSO SHOWN

case	plasma density	time-average	sheath thickness/
	at top boundary	sheath thickness*	trench width
	$n_o$ ( $\text{m}^{-3}$ )	$L_{sh}$ ( $\mu\text{m}$ )	$L_{sh}/D$
(a)	$1 \times 10^{18}$	108	0.216
(b)	$5 \times 10^{16}$	468	0.936
(c)	$6 \times 10^{15}$	1281	2.562

\* The sheath edge was defined as the position where the relative net charge,  $(n_i - n_e)/n_i$  was equal to 0.01, with the densities determined by the fluid simulation. The time-average sheath thickness was calculated far away from the trench, where the sheath was 1-D.

the upper boundary. The RF plasma sheath evolved *self-consistently* in accordance with the specified plasma parameters ( $n_o$  and  $T_e$ ; effectively the local Debye length), and the boundary potentials (essentially the sheath potential).

The ion continuity equations [(1) and (2)] were discretized in space using a flux corrected transport finite-difference scheme [27], [28]. The time step was chosen so that the Courant–Friedrichs–Levy condition was satisfied. In this study, the Courant number was set to be less than 0.3 [29]. The time step was also set less than 1/200 of the RF cycle time (74 ns). At the end of each time step, Poisson's equation(3) was solved iteratively by a Newton-Raphson method combined with a conjugate gradient scheme to update the electric potential. The successive over-relaxation method with Chebychev acceleration was used to invert the Jacobian matrix [30]. Marching in time was continued until a periodic steady-state was reached. This normally required 100s of RF cycles.

## B. MC Simulation

If ion flow is collisionless, the ion energy and angular distribution functions at the substrate can, in principle, be calculated knowing the electric field profiles and the (input) ion distributions at the upper boundary. When ions suffer collisions, however, MC simulation is necessary to calculate the ion distributions at the substrate. The MC simulation procedure has been described in detail before [5], and only a brief summary will be given here. For the flight between collisions (free flight) the equations of motion were integrated using a fourth-order Runge–Kutta method using the electric field profiles obtained by the fluid simulation. Ions with the appropriate energy and angular distributions [5] were launched near the sheath edge. The launching location was a horizontal plane in the presheath region. Ions were evenly distributed along the launching plane as well as in RF phase (0 to  $2\pi$ ). The position of the launching plane did not influence the results significantly, provided that the launching plane was far enough from the sheath edge.

During their transit through the sheath, ions can experience elastic scattering or charge-exchange collisions with the background gas. The null collision method was employed [31], with a constant total cross section, to evaluate the free flight distance between collision events. At the end of each free flight, the

type of collision was determined according to the probability for each collision event: elastic scattering, charge-exchange, and null collision. Collision cross sections were obtained from [1, p. 78]. Elastic scattering was treated as a hard sphere collision. For charge-exchange collisions, the fast ion and slow neutral switched identity (i.e., became fast neutral and slow ion, respectively) without changing their precollision velocity vector (resonant process). Both the fast neutral and slow ion were followed after the collision. Energetic neutrals could also suffer elastic scattering. Energetic particle (ions or fast neutrals) scattering on the Si surface is quite complicated [32]. Incidence angle, energy, and surface condition (roughness, contamination) all play a role. Several experimental and/or computational studies [33]–[36] have been reported on the impact of energetic ( $1 < \varepsilon_i < 1$  keV) ions on surfaces. The employed model for surface scattering is the simplest possible, consistent with current knowledge. When impacting ions lose most of their energy through a series of collisions with surface atoms, ions can be trapped in the surface. Trapped ions were not followed in the simulation. The probability for surface trapping was treated as a linear function of incidence angle, without energy dependency [35]. In case of reflection, the degree of ion neutralization was assumed to be 100% [1, p. 280] with specular reflection. To calculate the energy transfer, a binary collision model with two half-scatterings was employed [35]. This model assumes that the incident particle experiences two consecutive binary collisions with surface atoms, before being released from the surface. The scattering angle was assumed to be the same for both collisions. MC kinetic data for ions and fast neutrals were collected and recorded at the bottom of the trench.

### III. EXPERIMENTAL APPARATUS

The experimental data presented in this work was taken in a Gaseous Electronics Conference (GEC) reference cell [37] that had been modified to allow production of inductively-driven discharges [38]. Fig. 3 shows a schematic of the Cell, which has been extensively described previously [39]. A five-turn spiral RF-induction coil above the fused silica window on top of the cell was driven at a frequency of 13.56 MHz to excite the plasma. A 15-cm-diameter chuck at the bottom of the discharge was almost entirely covered with a heavily doped ( $0.005 \Omega\text{-cm}$ ) single-crystal Si wafer or wafer sections. A small segment of wafer containing a 1-mm-wide, 1-cm-long trench etched completely through the 540-micron-thick wafer was glued to a removable section of the chuck with conductive epoxy. A pinhole located in the bottom of this trench acted as the sampling aperture for these experiments, allowing ions that reached the bottom of the wafer to enter a separate vacuum system containing the ion analyzer. The  $6\text{-}\mu\text{m}$ -diameter pinholes were in nickel foils estimated by the manufacturer to be  $2\text{--}3 \mu\text{m}$  thick. The pinhole was moved relative to the trench wall by gluing different 1-mm-wide trenches down at different positions relative to nominally identical pinholes. In all cases, the pinhole remained centered over the analyzer.

When the chuck was RF biased at 13.56 MHz, it was phase-locked to the induction coil. A double Langmuir probe was used to measure the plasma density and electron temperature [40]–[42]. The RF component of the plasma potential was mea-

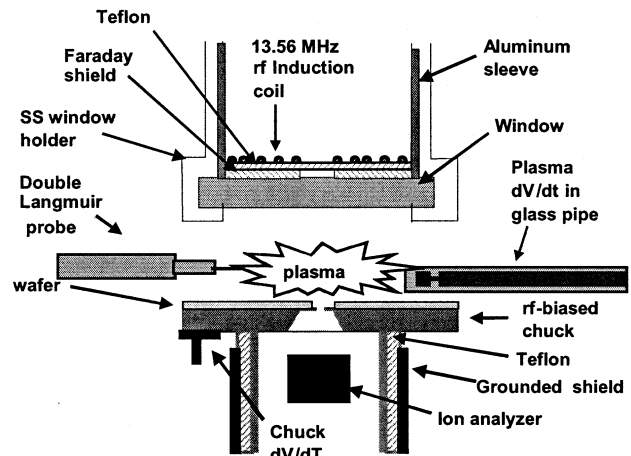


Fig. 3. Schematic of inductively coupled GEC Reference Cell with RF-biased wafer chuck. The ion analyzer looks through a  $6\text{-}\mu\text{m}$ -diameter pinhole in the chuck to view the ions impacting the wafer.

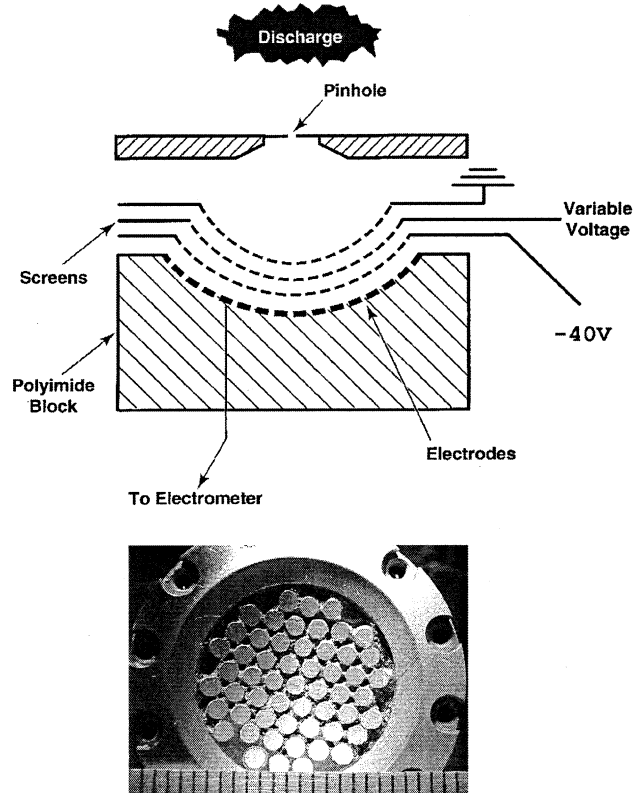


Fig. 4. Schematic of three-screen gridded ion analyzer. The grid nearest the pinhole was tied to local ground—the wall of the RF-biased chuck—to create a field-free drift region between the pinhole and the first screen. A front view of the 55 collector elements in the detector is also shown. The bundle of collector elements was 2.5 cm in diameter.

sured with a cylindrical capacitive voltage probe inside a glass pipe that was immersed in the plasma. The RF component of the voltage on the wafer chuck was measured with a Kapton-insulated capacitive probe held against the bottom of the chuck.

Fig. 4 shows a schematic of the gridded ion energy and angle analyzer probe used in this work. Probes of this type have been described in detail previously [39], [43]. Due to their hemispherical layout, these analyzers can measure ion fluxes, ion energies, and ion angular distributions. This particular analyzer dif-

fered from previous analyzers by having 55 current collector pins stacked in a hexagonal close-packed array also shown in Fig. 4. Thirty two of the collector pins, located either near the middle of the analyzer or on the side of the analyzer we expected the beam to be deflected toward, were monitored independently. The sum of the currents on the remaining 23 pins was also monitored to verify the way which ion trajectories were deflected.

Control voltages on the two screens and collector currents were passed through a 35-pin vacuum feedthrough to the inside of a copper box that floated at the RF and dc chuck potentials. This copper box contained power supplies for the control voltages as well as a low-current switching array that connected one collector pin at a time to a picoammeter. All these instruments were floating at the chuck potential, and they were powered by a battery. Signals were conveyed to and from a grounded laboratory computer via a fiber optic link. The electrically-floating copper box was surrounded by (but was electrically isolated from) a grounded copper box to protect the computer and the experimenters.

#### IV. RESULTS AND DISCUSSION

The main parameters varied in the simulation were the plasma density at the upper boundary (Fig. 2) of the computational domain,  $n_o$  ( $3 \times 10^{15}$  to  $2.5 \times 10^{18} \text{ m}^{-3}$ ) and the width of the trench,  $D$  (300, 500, and  $1000 \mu\text{m}$ ). The depth of the trench was either 500 or  $540 \mu\text{m}$ ; the latter was used for comparison with experiments. Other parameters were set at the base values shown in Table I. Three cases of  $n_o$  and the resulting sheath thickness are shown in Table II. When the electron temperature and sheath potential are fixed, the sheath thickness scales approximately as  $L_{sh} \sim n_o^{-1/2}$ . The ratio  $L_{sh}/D$  ranged from 0.152 up to 3.64.

##### A. Electric Potential and Field Profiles

Fig. 5 displays electric potential profiles for a  $500\text{-}\mu\text{m}$ -wide and  $500\text{-}\mu\text{m}$ -deep trench, for three different  $L_{sh}/D$  ratios. Cases (a)–(c) of Fig. 5 correspond to (a)–(c) of Table II, respectively. The time-average sheath thickness was calculated on the wall far away from the trench (1-D sheath), under otherwise identical conditions. The sheath thickness is smaller than, comparable to, and larger than the trench width for cases (a), (b), and (c), respectively. As a result, plasma molds along the surface topography of the trench, especially for case (a). In all cases, the sheath is locally thicker over the trench mouth and becomes thinner and planar away from the trench. As the ratio  $L_{sh}/D$  decreases [from (c)–(a)], the sheath becomes more conformal to the surface topography.

Figs. 6 and 7 show the resulting electric field vector and electric field strength profiles, respectively. Fig. 7 also shows sample ion streamlines. The electric field becomes significant within the sheath and increases toward the wall. Away from the trench, the electric field is vertical (1-D) and the field strength depends on the sheath potential (difference of potential between plasma and wall) and thickness. Near the trench, however, the electric field becomes 2-D due to plasma molding. The maximum of the electric field is seen at the corner of the mouth of the trench. Since ions gain most of their kinetic energy in the sheath, the ion flux, IEDs, and IADs along the trench surface contour depend on the deformed electric field. For a small sheath thick-

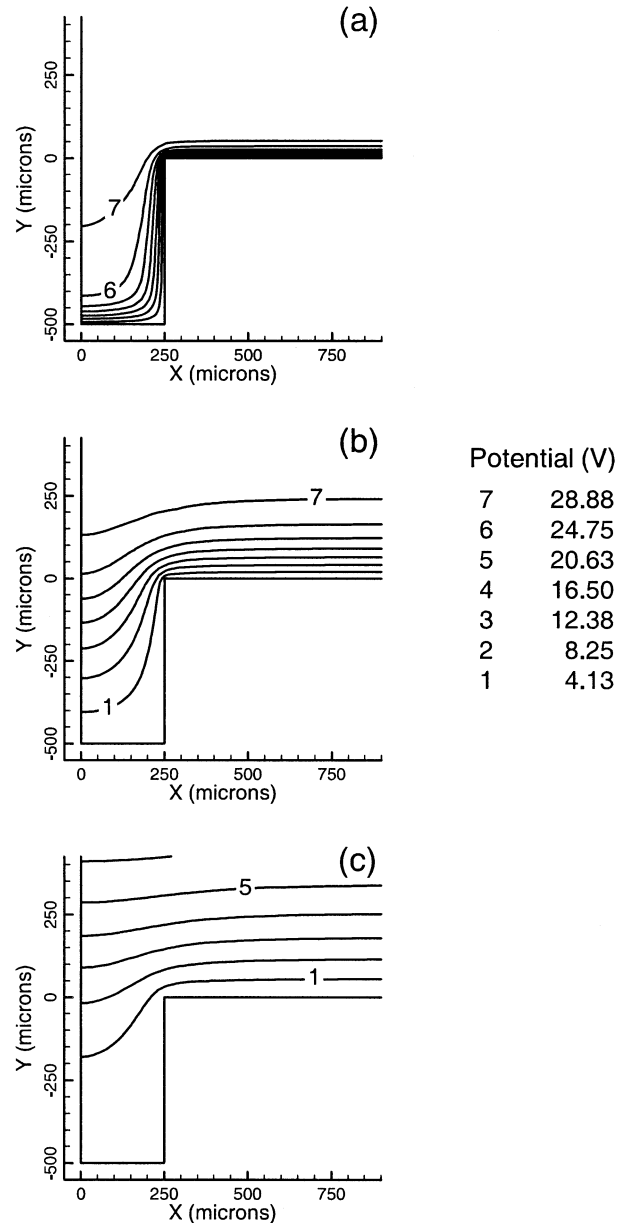


Fig. 5. Electric potential contours around a  $500\text{-}\mu\text{m}$ -wide and  $500\text{-}\mu\text{m}$ -deep trench at  $\tau_{RF} = 0$ . (a)  $L_{sh} = 108 \mu\text{m}$  ( $L_{sh}/D = 0.216$ ), (b)  $L_{sh} = 468 \mu\text{m}$  ( $L_{sh}/D = 0.936$ ), and (c)  $L_{sh} = 1281 \mu\text{m}$  ( $L_{sh}/D = 2.562$ ). Cases (a)–(c) correspond to (a)–(c), respectively, of Table II.  $L_{sh}$  is the time-average sheath thickness calculated far away from the trench, where the sheath was 1-D.

ness (Fig. 7(a),  $L_{sh}/D = 0.216$ ), the ion streamlines are drastically deformed inside the sheath, and a significant portion of ions strike the sidewall of the trench with a large impact angle (with respect to the  $y$  axis). When the sheath thickness is larger than the width of the trench (Fig. 7(c),  $L_{sh}/D = 2.562$ ), plasma molding is weaker and a smaller portion of the sheath is deformed by the presence of surface topography. In this case, ions spend a significant amount of their sheath transit time in a region of vertical electric field. Due to their vertical momentum, ions are not affected as strongly by the horizontal electric field near and inside the trench. Consequently, the impact angle (with respect to the  $y$  axis) and the flux of ions at the sidewall both decrease with increasing  $L_{sh}/D$ .

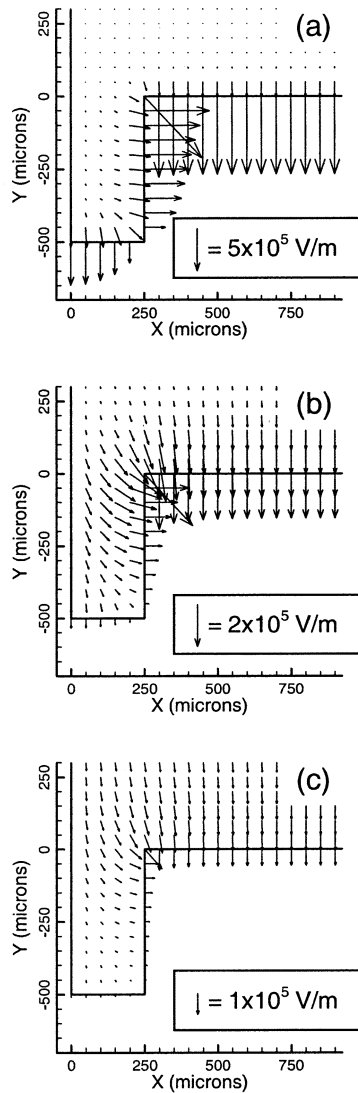


Fig. 6. Electric field vector plots for the conditions of Fig. 5: (a)  $L_{sh} = 108 \mu\text{m}$  ( $L_{sh}/D = 0.216$ ), (b)  $L_{sh} = 468 \mu\text{m}$  ( $L_{sh}/D = 0.936$ ), (c)  $L_{sh} = 1281 \mu\text{m}$  ( $L_{sh}/D = 2.562$ ).

### B. Distribution of Ion Flux

Fig. 8 shows the time-average ion flux along the surface contour of the trench, starting from the center of the trench bottom (point O, see inset figure). The ion flux was normalized by the value of the ion flux on the flat horizontal surface away from the trench. Since only the normal component of the flux is shown ( $n_i v$  for horizontal surfaces and  $n_i u$  for vertical surfaces), the flux is discontinuous at the two corners (points P and Q). Again, cases (a)–(c) of Fig. 8, correspond to (a)–(c), respectively, of Table II. For small values of  $L_{sh}/D$  (case a), the flux increases drastically along the horizontal surface from its undisturbed value, to a maximum at point Q. Along the sidewall QP, the ion flux shows a local maximum near (but not at) the upper corner Q, due to the inertia of incoming ions. As the ratio  $L_{sh}/D$  increases, the vertical inertia of oncoming ions becomes more significant. Thus, the maximum of ion flux on surfaces RQ and QP becomes less pronounced. Also, the location of the maximum shifts away from the corner point Q. The flux along the bottom of the trench shows a maximum at the center

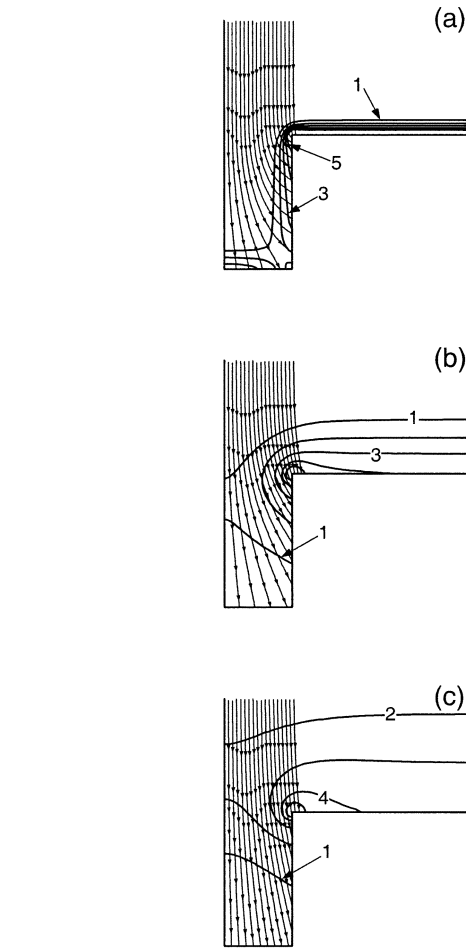


Fig. 7. Electric field strength contours and ion streamlines for the conditions of Fig. 5. The electric field strength  $(E_x^2 + E_y^2)^{1/2}$  was normalized by its maximum value ( $E_{max}$ ). (a)  $E_{max} = 11.45 \times 10^5 \text{ V/m}$ , (b)  $E_{max} = 4.265 \times 10^5 \text{ V/m}$ , and (c)  $E_{max} = 1.595 \times 10^5 \text{ V/m}$ . Contour level 5 = 0.625, level 4 = 0.5, level 3 = 0.375, level 2 = 0.25, level 1 = 0.125.

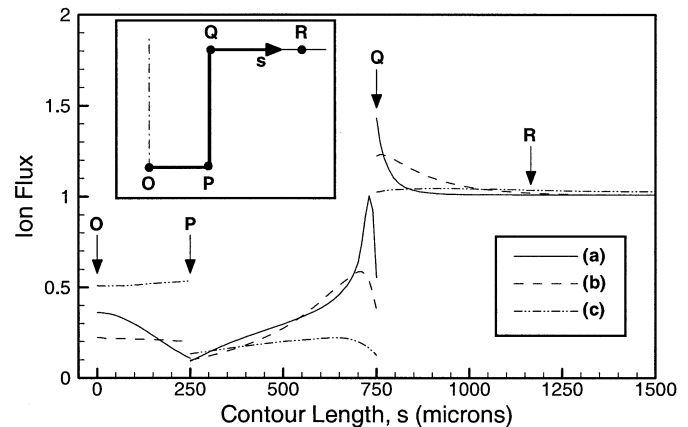


Fig. 8. Time-average ion flux as a function of contour length along the surface of the trench under the conditions of Fig. 5. The flux was normalized by its undisturbed value far away from the trench, where the sheath was 1-D: (a)  $2.14 \times 10^{21} \text{ m}^{-2}\text{s}^{-1}$ , (b)  $1.1 \times 10^{20} \text{ m}^{-2}\text{s}^{-1}$ , and (c)  $1.43 \times 10^{19} \text{ m}^{-2}\text{s}^{-1}$ . The flux normal to surface is shown, i.e.,  $n_i v$  for horizontal surfaces (OP and QR) and  $n_i u$  for sidewall (PQ), where  $n_i$  is the ion density and  $u$  and  $v$  are the horizontal and vertical components of the ion fluid velocity, respectively. The contour length  $s$  was measured from point O (center of the trench bottom) along the surface as displayed by the thick arrow of the insert.

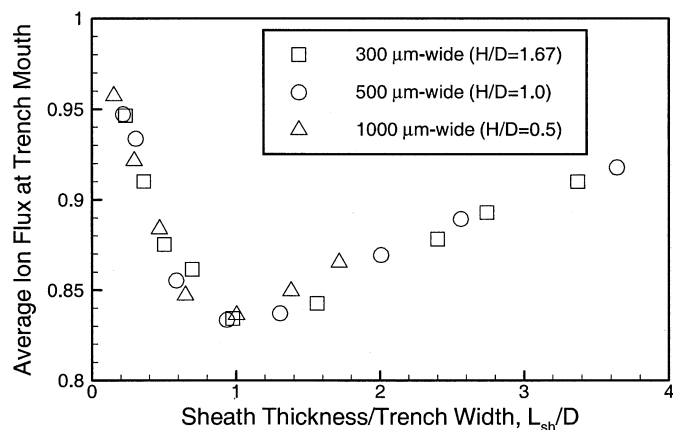


Fig. 9. Time-and-space-average ion flux at the mouth of 500  $\mu\text{m}$ -deep trenches as a function of  $L_{sh}/D$ . The flux was normalized by its undisturbed value far away from the trench, where the sheath was 1-D.

(point O) for case (a) and monotonically decreases toward the corner (point P). The flux is relatively uniform for the thicker sheath cases (b) and (c).

Ions passing beyond the mouth of a trench will strike either the bottom or the sidewall of the trench. Due to the diverging flow of ions, the average flux at the mouth of the trench may be less than the undisturbed value (i.e., the flux on a flat wall). The average (both time and space) ion flux at the *mouth* of a trench as a function of the ratio  $L_{sh}/D$  is displayed in Fig. 9. The flux was again normalized by its undisturbed value, calculated under otherwise identical conditions. Three 500- $\mu\text{m}$ -deep trenches with different widths (300, 500, and 1000  $\mu\text{m}$ ) were simulated. The aspect ratio, depth/width ( $= H/D$ ), of the trenches was 1.67, 1.0, and 0.5, respectively. Irrespective of the aspect ratio, the average ion flux at the trench *mouth* depends only on the ratio  $L_{sh}/D$ . The flux shows a minimum of 0.83 at  $L_{sh}/D \sim 1.0$ . For very large  $L_{sh}/D$  [see also Fig. 1(c)], the ion flow is mainly vertical, and it is hardly affected by the presence of the trench. In this case, the flux at the mouth should approach the undisturbed value (i.e., a normalized flux of 1.0). As  $L_{sh}/D$  decreases, the horizontal electric field becomes strong enough to induce significant ion divergence, reducing the flux at the mouth. At the other extreme of very small  $L_{sh}/D$  [see also Fig. 1(a)], however, the flux increases again because the sheath clings close to the surface and, thus, occupies a very small fraction of the mouth area of the trench.

Fig. 10 shows the average (time and space) ion flux at the trench *bottom* versus  $L_{sh}/D$  (with the trench width as a parameter) under the same conditions as in Fig. 9. For a given trench width, the behavior of ion flux versus  $L_{sh}/D$  is similar to that of Fig. 9. However, the flux at the bottom strongly depends on the width (aspect ratio) of the trench. As the aspect ratio increases, fewer ions arrive at the bottom due to the diverging flow of ions inside the trench. The flux at the bottom shows a minimum at lower values ( $\sim 0.5$ ) of  $L_{sh}/D$  compared to the flux at the mouth. This is because the divergence of ion flow is further enhanced by the horizontal electric field *inside* the trench (see Fig. 6).

### C. Ion Energy and Angular Distributions Along the Trench Bottom

The energy distributions of ions impinging on the bottom of the trench are shown in Fig. 11(a)–(c), which correspond to

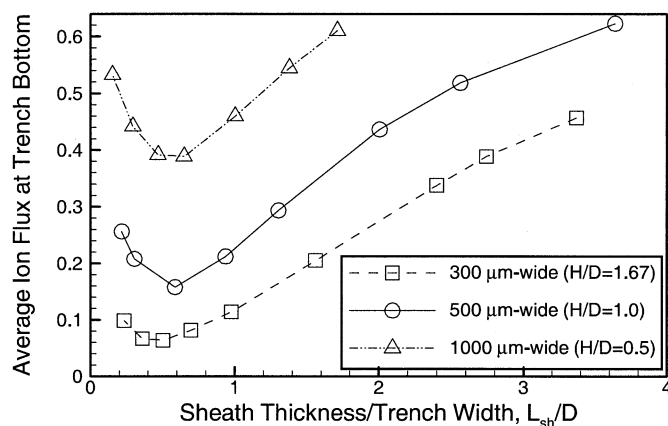


Fig. 10. Time-and-space-average ion flux at the bottom of 500  $\mu\text{m}$ -deep trenches versus  $L_{sh}/D$ . The flux was normalized by its undisturbed value far away from the trench, where the sheath was 1-D.

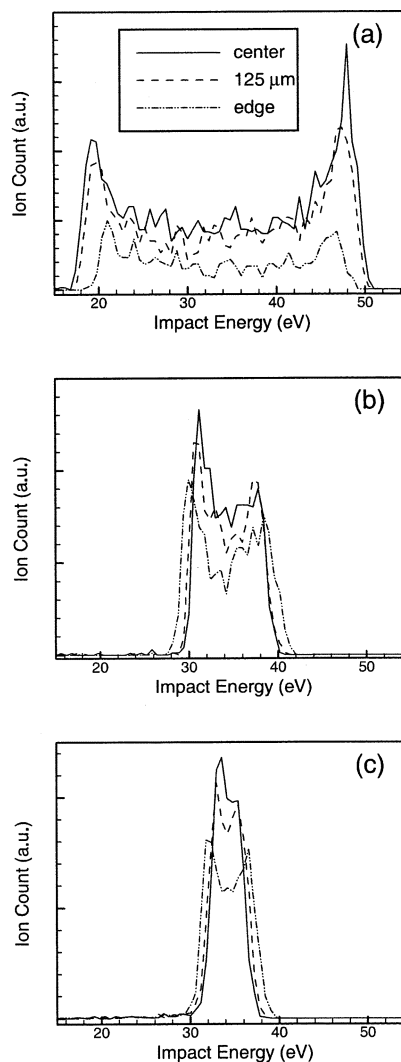


Fig. 11. Ion energy distributions at three locations of the trench bottom. Cases (a)–(c) correspond to (a)–(c) of Fig. 5.

cases (a)–(c), respectively, of Fig. 5 (and Table II). The IEDs were calculated using the MC simulation with the RF electric field profiles found by the fluid simulation as input (the elec-

tric field profiles at  $\tau_{RF} = 0$  are shown in Fig. 6). Fig. 11 depicts IEDs at three locations of the bottom surface: center (point O of Fig. 8), edge (point P), and 125  $\mu\text{m}$  (midpoint between point O and P). The shape of the IEDs depends on a ratio of the ion transit time in the sheath ( $\tau_{ion}$ ) to the RF period of the sheath potential ( $\sim 1/\omega_{RF}$ ) [11]. When  $\tau_{ion}\omega_{RF} \ll 1$ , ions cross the sheath in a small fraction of the RF period, and experience the instantaneous potential drop of the sheath, thus having a double peaked energy distribution. The energy spread,  $\Delta E$ , can be as large as the peak-to-peak RF sheath potential [17]. When  $\tau_{ion}\omega_{RF} \gg 1$ , ions spend long enough time inside the sheath to be accelerated by the time-average sheath potential. In this case, the resulting IEDs are single peaked. For a thinner sheath [Fig. 11(a)], the ion transit time is shorter, and ions have typical bicornuate (double peaked) IEDs with larger  $\Delta E$  ( $\sim 30$  eV). As the sheath thickens and  $\tau_{ion}$  increases, the IEDs narrow (case b,  $\Delta E \sim 7$  eV) and eventually, become nearly single peaked (case c). Interestingly, for small  $L_{sh}/D$  (case a),  $\Delta E$  decreases as one goes from the center to the edge at the bottom of the trench. For small  $L_{sh}/D$ , the sheath is slightly thicker near the edge (compared to the center), resulting in a bit larger  $\tau_{ion}\omega_{RF}$ , and thus smaller  $\Delta E$ . In contrast,  $\Delta E$  increases as one goes from the center to the edge in cases (b) and (c). In these cases of thicker sheath, variations of sheath thickness are not as important along the bottom of the trench. However, ions that finally land near the bottom edge are likely to have experienced a larger modulation of the electric field, leading to larger  $\Delta E$ .

The corresponding ion angular distributions are shown in Fig. 12(a)–(c). At the center of the bottom of the trench (solid lines), the IADs are nearly Gaussian, with a spread of several degrees off normal. As the edge is approached, however, ions sample an electric field with a progressively stronger horizontal component, thus having larger impact angles. The divergence of ion flow is less pronounced as the sheath becomes thicker [cases (b) and (c)], resulting in smaller impact angles at the off-center locations (125  $\mu\text{m}$  and edge) and a less nonuniform ion flux.

#### D. Flux of Energetic Neutrals at the Bottom of the Trench

As seen from Figs. 9 and 10, a significant portion of the ion flux strikes the trench sidewall. Unless ions are trapped in the surface, they will be reflected as energetic neutrals and may impinge on the trench bottom or opposite sidewall (for high aspect ratio trenches). The flux profiles (top) and the average flux and impact energy (bottom) of fast neutrals impinging on the bottom of the 500- $\mu\text{m}$ -wide and 500- $\mu\text{m}$ -deep trench are shown as a function of the sheath thickness in Fig. 13. The neutral flux was normalized by the value of the undisturbed ion flux on a flat surface far away from the trench. As the sheath gets thinner, the maximum of the neutral flux is seen further away from the sidewall (top). This is due to the fact that the impact angle (with respect to the  $y$  axis) of ions striking the sidewall is increasing with decreasing  $L_{sh}$  (see Figs. 7 and 12). Thus, specularly reflected neutrals strike the bottom of the trench further away from the sidewall. The flux profile becomes quite uniform for  $L_{sh} = 108$   $\mu\text{m}$ . It should be noted that, for small sheath thickness, the neutral flux can be reduced as a result of surface trapping of ions. Once trapped in the surface, ions eventually

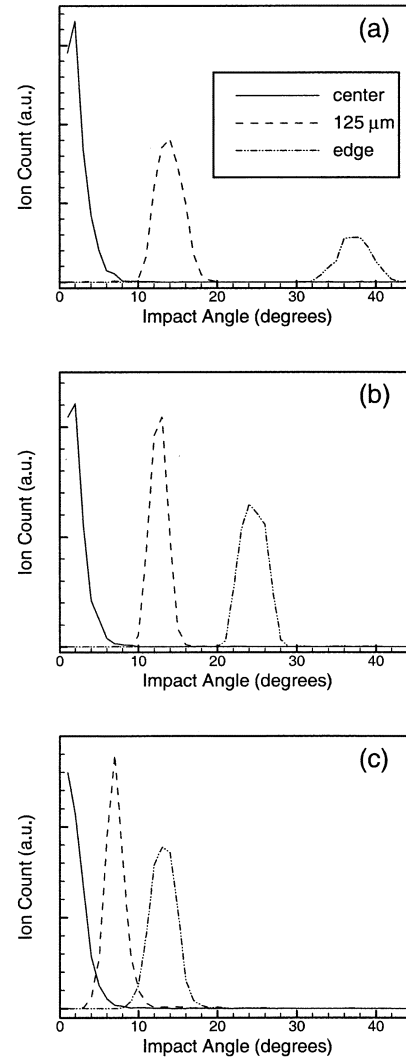


Fig. 12. Ion angular distributions at three locations of the trench bottom. Cases (a)–(c) correspond to (a)–(c) of Fig. 5.

reappear as *thermal* neutrals, and not as energetic neutrals of interest to this work. The dependence of the (average) neutral flux on sheath thickness (bottom figure) reflects the trends found in Figs. 9 and 10, since the neutral flux at the bottom scales with the difference between the *ion* flux at the mouth and bottom of the trench. For thick sheaths, the neutral flux is low since ions are more directional and fewer ions strike the sidewall to yield energetic neutrals. For thin sheaths, the neutral flux is again low mainly due to ion trapping on the sidewall. The trapping probability is higher for ions impinging closer to the normal on the sidewall, and thin sheaths favor such impact angles (Figs. 7 and 12). The maximum value of the normalized neutral flux is about 0.56 (at  $L_{sh}/D \sim 0.6$ ). For large sheath thickness ( $L_{sh}/D \geq 2$ ), the neutrals retain about 70% of the dc part of the sheath potential. As the sheath thickness decreases, ions strike the sidewall closer to normal incidence, more energy is lost upon impact, and the average energy of the emerging fast neutrals progressively decreases. It should be noted that the vast majority of fast neutrals formed as a result of ion reflection on the sidewalls. The fraction of fast neutrals formed in the gas phase by charge exchange was unimportant under these conditions.

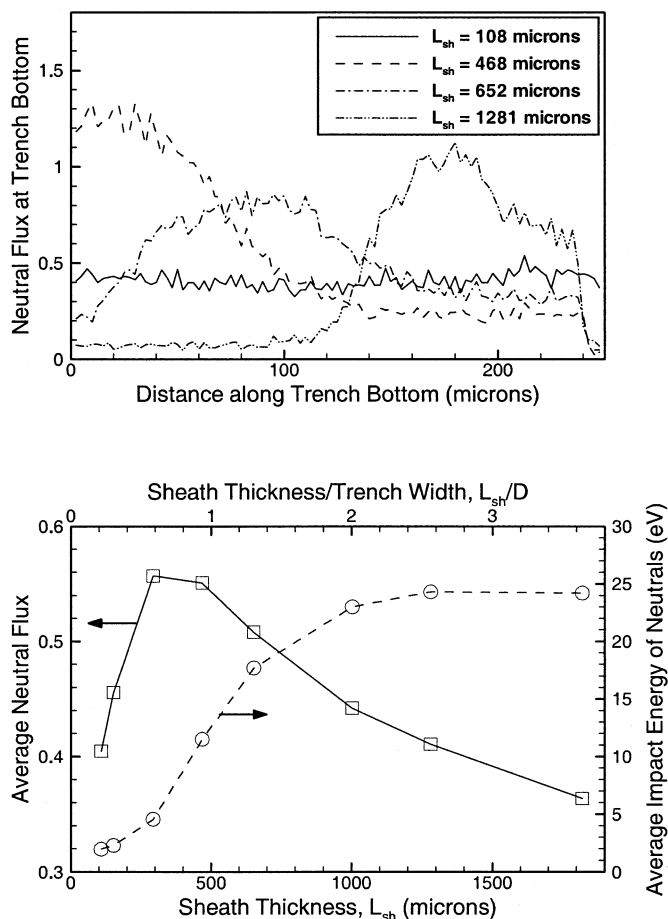


Fig. 13. (top) Time-average flux of energetic (fast) neutrals as a function of position along the bottom of a trench ( $500\text{-}\mu\text{m}$ -wide and  $500\text{-}\mu\text{m}$ -deep). Position zero corresponds to the center of the trench bottom. (bottom) Time- and space-average flux and impact energy of energetic neutrals at the same trench bottom as a function of sheath thickness. In all cases, the neutral flux was normalized by the undisturbed value of the ion flux far away from the trench, where the sheath was 1-D.

### E. Comparison With Experimental Measurements

Ion distributions in Ar plasmas were measured at the bottom of  $1000\text{-}\mu\text{m}$ -wide and  $540\text{-}\mu\text{m}$ -deep trenches, using the experimental apparatus described in Section III. The pinhole was placed at four different locations: 0, 200, 330, and  $436\text{ }\mu\text{m}$  away from the center of the trench bottom.

Simulation results were compared with experimental data for two sets of conditions. With 2.5 mtorr Ar gas pressure and 100 W induction coil power, the plasma density was  $3.42 \times 10^{16}\text{ m}^{-3}$ , and the electron temperature was 3.65 eV (as measured by a floating double probe). When RF biased, the peak-to-peak voltage between the plasma and the chuck was  $92\text{ V}_{\text{pp}}$ . The potential values used for the simulation were  $\Phi_o = 80 + 46\sin\omega_{\text{RF}}t\text{ V}$  ( $f_{\text{RF}} = 13.56\text{ MHz}$ ) for the RF biased case and  $\Phi_o = 25\text{ V}$  for the unbiased case (the measured average ion energy was used as an estimate of the dc plasma potential). The second experiment was performed with 10-mtorr Ar gas pressure and 200 W induction coil power. The corresponding plasma density and electron temperature were  $1.6 \times 10^{17}\text{ m}^{-3}$  and 2.7 eV, respectively. When the chuck was RF biased, the peak-to-peak

TABLE III  
PARAMETER VALUES FOR COMPARING SIMULATION TO EXPERIMENTS. TRENCHES WERE  $1000\text{-}\mu\text{m}$ -WIDE AND  $540\text{-}\mu\text{m}$ -DEEP. WHEN BIASED, THE RF FREQUENCY OF THE PLASMA POTENTIAL WAS 13.56 MHz. THE POTENTIAL OF THE WALL  $\Phi_w$  WAS SET AT 0 V FOR ALL CASES. FOR OTHER PARAMETER VALUES, SEE TABLE I

pressure, power	plasma density at upper boundary $n_o\text{ (m}^{-3}\text{)}$	electron temperature (eV)	potential at upper boundary $\Phi_o\text{ (V)}$	sheath thickness $L_{sh}\text{ (}\mu\text{m)}$
2.5mT, 100W	$3.42 \times 10^{16}$	3.65	$80 + 46\sin\omega_{\text{RF}}t$	755
			25 (DC)	476
10mT, 200W	$1.6 \times 10^{17}$	2.7	$73 + 44\sin\omega_{\text{RF}}t$	377
			25 (DC)	238

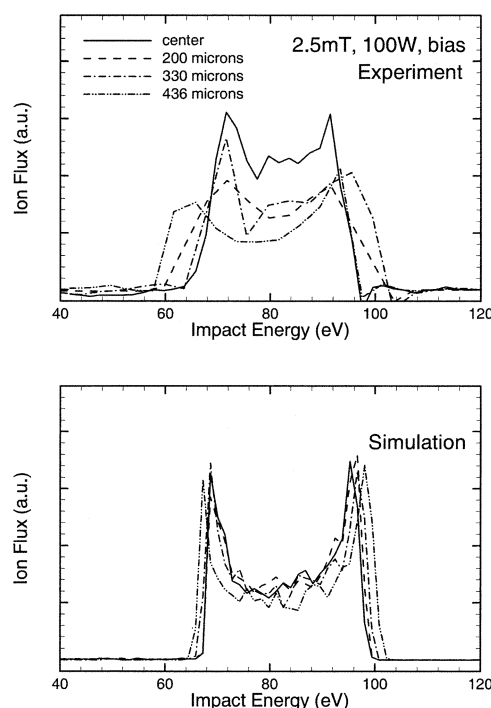


Fig. 14. Comparison between experimental data and simulation predictions of ion energy distributions at four different locations at the trench bottom for 2.5-mtorr pressure and 100-W induction coil power and with RF bias. Distances are from the center of the trench bottom. See Table III for other conditions. In this case, where the sheath thickness is comparable to the trench width, both experiments and data show that the IEDs are narrowest at the center of the trench.

voltage between the plasma and the chuck was  $88\text{ V}_{\text{pp}}$ . The potential values used for the simulation for this case were  $\Phi_o = 73 + 44\sin\omega_{\text{RF}}t\text{ V}$  ( $f_{\text{RF}} = 13.56\text{ MHz}$ ) for the RF biased chuck and  $\Phi_o = 25\text{ V}$  for the unbiased chuck. The parameter values used in the simulation for each case and the resulting sheath thickness are summarized in Table III.

Figs. 14 and 15 compare simulated and measured ion energy distributions at the bottom of the trench. Overall, the simulation results are in good agreement with the experimental measurements. All qualitative trends are captured. When the ratio  $L_{sh}/D$  is relatively large, the double peaked IEDs narrow as one approaches the center of the trench (2.5-mtorr case, Fig. 14).

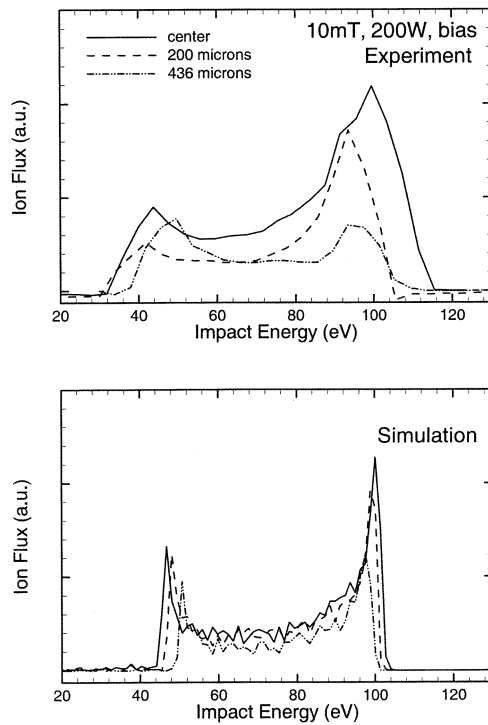


Fig. 15. Comparison between experimental data and simulation predictions of ion energy distributions at three different locations at the trench bottom for 10-mTorr pressure and 200-W induction coil power and with RF bias. Distances are from the center of the trench bottom. See Table III for other conditions. In this case, where the sheath thickness is smaller than the trench width, both experiments and data show that the IEDs are broadest at the center of the trench.

The reverse situation happens for relatively small  $L_{sh}/D$  (10-mTorr case, Fig. 15, see also Fig. 11). The finite energy resolution of the analyzer ( $\sim 2$  eV at 40 eV and  $\sim 5$  eV at 100 eV) is partly responsible for the broader peaks seen in the experimental data.

Figs. 16 and 17 compare simulated and measured ion angular distributions at the trench bottom. Since each of the current collection pins subtended  $\sim 7^\circ$  as seen from the pinhole, the flat-topped experimental curves can only indicate how much flux is within each  $7^\circ$ -wide "bin." The trends of ion angular distribution versus distance from the center of the 1-mm-wide trench are identical in the simulations and experimental data. As the wall is approached, ions are subjected to stronger deflection, resulting in larger impact angles on the bottom surface (with respect to the vertical).

Fig. 18 compares simulated and measured ion fluxes. Again, data and simulations show the same trend, a decrease in ion flux as the sampling point nears the wall. When a bias voltage is applied and the sheath grows, the vertical momentum of the incoming ions is stronger compared to the horizontal component, resulting in more uniform ion flux at the trench bottom (the apparent minimum of the experimental ion flux at 10 mTorr with bias does not seem to be significant). It is instructive to look at the dependence of ion flux on the ratio  $L_{sh}/D$  in view of the results of Fig. 10. At 10 mTorr, the sheath thickness was predicted to increase from 238 (without bias) to 377  $\mu\text{m}$  (with bias, see Table III). The corresponding  $L_{sh}/D$  ratios (0.238 without bias and 0.377 with bias) are located to the left of the minimum in Fig. 10. Thus, the ion flux at the trench bottom de-

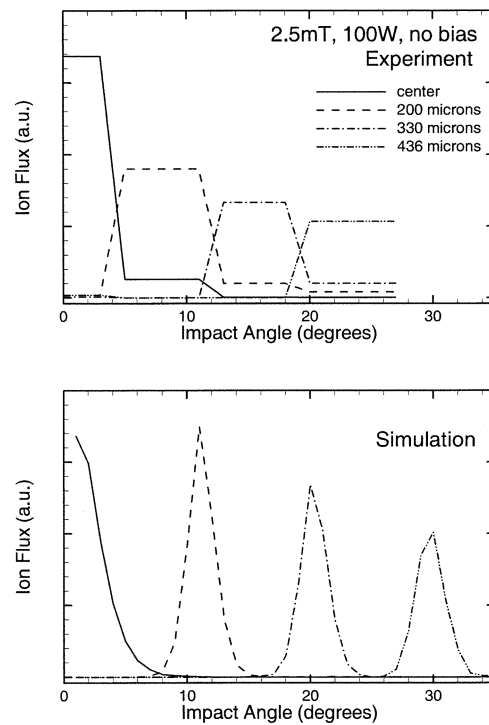


Fig. 16. Comparison between experimental data and simulation predictions of ion angular distributions at four different locations at the trench bottom for 2.5-mTorr pressure and 100-W induction coil power with no RF bias. Distances are from the center of the trench bottom. See Table III for other conditions.

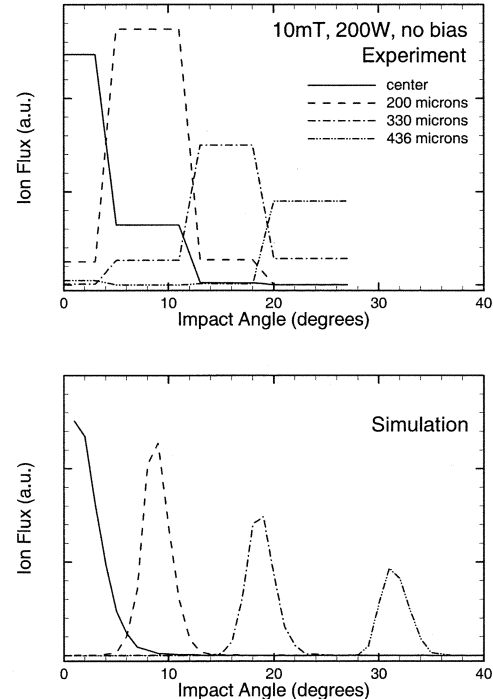


Fig. 17. Comparison between experimental data and simulation predictions of ion angular distributions at four different locations at the trench bottom for 10-mTorr pressure and 200-W induction coil power with no RF bias. Distances are from the center of the trench bottom. See Table III for other conditions.

creases as the sheath grows with applied bias. This is predicted by the simulation and verified by the data of Fig. 18, top. On the other hand, at 2.5 mTorr,  $L_{sh}/D$  varies from 0.476 (without

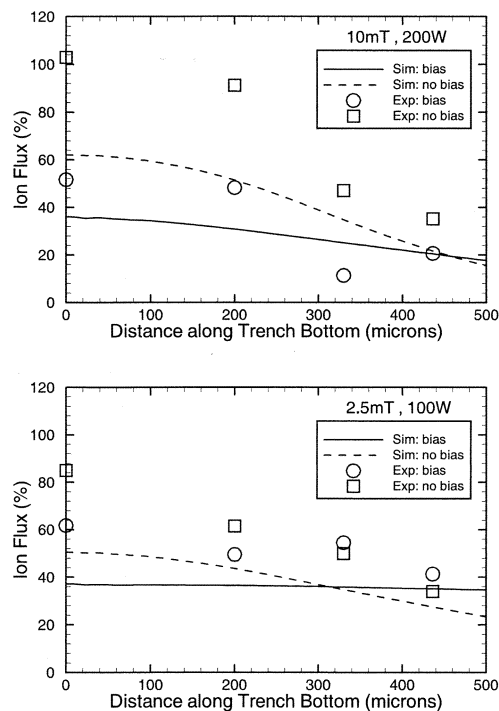


Fig. 18. Comparison between experimental data and simulation predictions of ion flux distributions along the trench bottom. For each set of conditions (pressure, power, and bias) the flux was normalized by the undisturbed value on a flat wafer under the same set of conditions. See Table III for other conditions.

bias) to 0.755 (with bias), i.e.,  $L_{sh}/D$  is around its minimum value in Fig. 10. Therefore, the ion flux at the trench bottom does not change appreciably as bias is applied under this condition (Fig. 18 bottom).

Overall, the simulation results are in very good qualitative agreement with the experimental measurements. Considering experimental uncertainties (normally a factor of two in the ion density, for example), the model predictions are also in reasonable quantitative agreement with the experimental data.

## V. SUMMARY AND CONCLUSION

A 2-D fluid/MC simulation was developed to study plasma molding over surface topography. The self-consistent fluid simulation included the ion mass and momentum continuity equations, coupled to the Poisson equation for the electric potential. The Boltzmann relation was assumed for electrons (no electron inertia), with a constant electron temperature. The simulation predicted the evolution of the RF plasma sheath over the surface topography, and the spatiotemporal profiles of the electric field in the region. Using the electric field profiles from the fluid simulation, ions, and energetic neutrals (resulting by ion neutralization on the wall or by charge exchange collisions in the gas phase) were followed by the MC simulation. With these simulation procedures, ion flow, and the energy and angular distribution functions of ions and energetic neutrals along the surface of a trench (width  $D$  and depth  $H$ ) were predicted.

As the sheath thickness  $L_{sh}$  decreased, the sheath edge became more conformal to the surface topography. The resulting strong horizontal component of electric field modified the ion trajectories, deflecting ions toward the trench sidewall. The

redistribution of the ion flux strongly depended on the ratio  $L_{sh}/D$ . For a relatively thin sheath, the ion flux along the surface contour showed a sharp maximum at the corner of the trench mouth. As the sheath thickness increased, the vertical inertia of oncoming ions became more significant, and the maximum of the ion flux was less pronounced. In addition, a more uniform flux of ions was found at the trench bottom for thicker sheaths. Irrespective of the trench depth, the average ion flux at the trench *mouth* showed a minimum at  $L_{sh}/D \sim 1.0$ , and approached the undisturbed value (that for a flat surface) at both extremes  $L_{sh}/D \ll 1$  and  $L_{sh}/D \gg 1$ . In addition to its dependence on  $L_{sh}/D$ , the average flux at the trench *bottom* was also affected by the trench depth  $H$ , with the flux decreasing as  $H/D$  increased. As the trench sidewall was approached, the energy spread  $\Delta E$  IEDs at the trench bottom decreased for a thin sheath, but increased for a thick sheath. The IADs at the trench bottom peaked at larger angles off normal as the trench sidewall was approached. The situation was exacerbated for thinner sheaths resulting in stronger deflection of ions. Ions striking the sidewall were assumed to reflect as energetic neutrals. At the trench bottom, the energetic neutral flux was comparable to the ion flux over the entire range of sheath thickness studied. The average energetic neutral flux at the trench bottom showed a maximum as a function of sheath thickness. However, the average energy of fast neutrals increased monotonically as the sheath thickness increased. Simulation results were in good agreement with experimental data on ion flux, IEDs and IADs at the trench bottom.

## REFERENCES

- [1] M. A. Lieberman and A. J. Lichtenberg, *Principles of Plasma Discharges and Materials Processing*. New York: Wiley, 1994.
- [2] I. W. Rangelow and H. Loschner, "Reactive ion etching for microelectrical mechanical system fabrication," *J. Vac. Sci. Technol. B*, vol. 13, pp. 2394–2399, 1995.
- [3] D. J. Economou and R. C. Alkire, "Effect of potential field on ion deflection and shape evolution of trenches during plasma-assisted etching," *J. Electrochem. Soc.*, vol. 135, pp. 941–949, 1988.
- [4] J. M. Lane, K. H. A. Bogart, F. P. Klemens, and J. T. C. Lee, "The role of feedgas chemistry, mask material, and processing parameters in profile evolution during plasma etching of Si(100)," *J. Vac. Sci. Technol. A*, vol. 18, pp. 2067–2079, 2000.
- [5] D. Kim and D. J. Economou, "Plasma molding over surface topography: Simulation of ion flow, and energy and angular distributions over steps in rf high density plasmas," *IEEE Trans. Plasma Sci.*, vol. 30, pp. 2048–2058, Oct. 2003.
- [6] J. R. Woodworth, P. A. Miller, R. J. Shul, I. C. Abraham, B. P. Aragon, T. W. Hamilton, C. G. Willison, D. Kim, and D. J. Economou, "Experimental and theoretical study of ion distributions near 300  $\mu\text{m}$  tall steps on rf-biased wafers in high density plasmas," *J. Vac. Sci. Technol. A*, vol. 21, pp. 147–155, 2003.
- [7] S. M. Rossnagel, J. J. Cuomo, and W. D. Westwood, Eds., *Handbook of Plasma Processing Technology*. Park Ridge, NJ: Noyes, 1990.
- [8] D. T. K. Kwok, X. Zenh, Q. Chen, P. K. Chu, and T. E. Sheridan, "Effects of tube length and radius for inner surface plasma immersion ion implantation using an auxiliary electrode," *IEEE Trans. Plasma Sci.*, vol. 27, pp. 225–238, Feb. 1999.
- [9] S. Panda, D. J. Economou, and L. Chen, "Anisotropic etching of polymer films by high energy ( $\sim 100$  eV) oxygen atom neutral beams," *J. Vac. Sci. Technol. A*, vol. 19, pp. 398–404, 2001.
- [10] P. A. Miller and M. E. Riley, "Dynamics of collisionless rf plasma sheaths," *J. Appl. Phys.*, vol. 82, pp. 3689–3709, 1997.
- [11] T. Panagopoulos and D. J. Economou, "Plasma sheath model and ion energy distribution for all radio frequencies," *J. Appl. Phys.*, vol. 85, pp. 3435–3443, 1999.

- [12] E. Kawamura, V. Vahedi, M. A. Lieberman, and C. K. Birdsall, "Ion energy distributions in rf sheaths; review, analysis and simulation," *Plasma Sources Sci. Technol.*, vol. 8, pp. R45–R64, 1999.
- [13] M. J. Kushner, "Distribution of ion energies incident on electrodes in capacitively coupled rf discharges," *J. Appl. Phys.*, vol. 58, pp. 4024–4031, 1985.
- [14] B. E. Thomson, H. H. Sawin, and D. A. Fisher, "Monte Carlo simulation of ion transport through rf glow-discharge sheaths," *J. Appl. Phys.*, vol. 63, pp. 2241–2251, 1988.
- [15] S. Kanakasabapathy and L. Overzet, "A coupled two-sheath simulation of rf bias at high electronegativities," *Plasma Sources Sci. Technol.*, vol. 7, pp. 289–297, 1998.
- [16] M. A. Sobolewski, J. K. Olthoff, and Y. Wang, "Ion energy distributions and sheath voltages in a radio-frequency-biased, inductively coupled, high-density plasma reactor," *J. Appl. Phys.*, vol. 85, pp. 3966–3975, 1999.
- [17] E. A. Edelberg, A. Perry, N. Benjamin, and E. S. Aydil, "Energy distribution of ions bombarding biased electrodes in high density plasma reactors," *J. Vac. Sci. Technol. A*, vol. 17, pp. 506–516, 1999.
- [18] J. R. Woodworth, M. E. Riley, P. A. Miller, G. A. Hebner, and T. W. Hamilton, "Ion energy and angular distributions in inductively driven discharges in chlorine," *J. Appl. Phys.*, vol. 81, pp. 5950–5959, 1997.
- [19] D. Bose, T. R. Govindan, and M. Meyyappan, "Ion dynamics model for collisionless radio frequency sheaths," *J. Appl. Phys.*, vol. 87, pp. 7176–7184, 2000.
- [20] K.-U. Riemann, "Bohm criterion and ion-acoustic sound barrier," *Phys. Fluids B*, vol. 3, pp. 3331–3338, 1991.
- [21] J. H. Whealton, D. K. Olsen, and R. J. Jaridson, "Toward a realistic and tractable model for negative-ion extraction from volume sources," *Rev. Sci. Instrum.*, vol. 69, pp. 1103–1105, 1998.
- [22] Y. El-Zein, A. Amin, C. Shen, S. Yi, and K. Lonngren, "Two-dimensional sheath evolution in a negative ion plasma," *J. Appl. Phys.*, vol. 79, pp. 3853–3860, 1996.
- [23] M. Hong and G. A. Emmert, "Two-dimensional fluid modeling of time-dependent plasma sheath," *J. Vac. Sci. Technol. B*, vol. 12, pp. 889–896, 1994.
- [24] I. J. Donnelly and P. A. Watterson, "Ion-matrix sheath structure around cathodes of complex shape," *J. Phys. D, Appl. Phys.*, vol. 22, pp. 90–93, 1989.
- [25] O. Domokan, "Ion-matrix sheaths related to targets with grooves," *J. Appl. Phys.*, vol. 91, pp. 5587–5591, 2002.
- [26] F. F. Chen, *Introduction to Plasma Physics and Controlled Fusion*. New York: Plenum, 1984, vol. 1, Plasma Physics.
- [27] J. P. Boris and D. L. Book, "Flux-corrected transport. I. SHASTA a fluid transport that works," *J. Comput. Phys.*, vol. 11, pp. 38–69, 1973.
- [28] S. T. Zalesak, "Fully multidimensional flux-corrected transport algorithm for fluids," *J. Comput. Phys.*, vol. 31, pp. 335–362, 1979.
- [29] P. J. Roache, *Fundamentals of Computational Fluid Dynamics*. Albuquerque, NM: Hermosa, 1998.
- [30] W. H. Press, S. A. Teukolsky, W. T. Vetterling, and B. P. Flannery, *Numerical Recipes in Fortran*. Cambridge, U.K.: Cambridge Univ. Press, 1992.
- [31] C. K. Birdsall, "Particle-in-cell charged-particle simulations, plus Monte Carlo collisions with neutral atoms," *IEEE Trans. Plasma Sci.*, vol. 19, pp. 65–85, Apr. 1991.
- [32] H. Niehus, W. Heiland, and E. Taglauer, "Low-energy ion scattering at surfaces," *Surf. Sci. Rep.*, vol. 17, pp. 213–303, 1993.
- [33] S. R. Kasi, M. A. Kilburn, H. Kang, J. W. Rabalais, L. Tavermini, and P. Hochmann, "Interaction of low energy reactive ions with surfaces. III. Scattering of 30–200 eV Ne<sup>+</sup>, O<sup>+</sup>, and CO<sup>+</sup> from Ni(111)," *J. Chem. Phys.*, vol. 88, pp. 5902–5913, 1988.
- [34] G. S. Hwang, C. M. Anderson, M. J. Gordon, T. A. Moore, T. K. Minton, and K. P. Giapis, "Gas-surface dynamics and profile evolution during etching of silicon," *Phys. Rev. Lett.*, vol. 77, pp. 3049–3052, 1996.
- [35] B. A. Helmer and D. B. Graves, "Molecular dynamics simulations of Ar<sup>+</sup> and Cl<sup>+</sup> impacts onto silicon surfaces: Distributions of reflected energies and angles," *J. Vac. Sci. Technol. A*, vol. 16, pp. 3502–3514, 1998.
- [36] W. Choi, C. Kim, and H. Kang, "Interactions of low energy (10–600 eV) noble gas ions with a graphite surface: Surface penetration, trapping and self-sputtering behaviors," *Surf. Sci.*, vol. 281, pp. 323–335, 1993.
- [37] P. J. Hargis, K. E. Greenberg, P. A. Miller, J. B. Gerards, J. R. Torczynski, M. E. Riley, G. A. Hebner, J. R. Roberts, J. K. Olthoff, J. R. Whetstone, R. J. VanBrunt, M. A. Sobolewski, H. A. Anderson, M. P. Splichal, J. L. Mock, P. Bletzinger, A. Garscadden, R. A. Gottscho, G. Selwyn, M. Dalvie, J. E. Heidenreich, J. W. Butterbaugh, M. L. Brake, M. L. Passow, J. Pender, A. Lujan, M. E. Elta, D. B. Graves, H. H. Sawin, M. J. Kushner, J. T. Verdeyen, R. Horwath, and T. R. Turner, "The gaseous electronics conference radio-frequency reference cell: A defined parallel-plate radio-frequency system for experimental and theoretical studies of plasma-processing discharges," *Rev. Sci. Instrum.*, vol. 65, pp. 140–154, 1994.
- [38] P. A. Miller, G. A. Hebner, K. E. Greenberg, P. D. Pochan, and B. P. Aragon, "An inductively coupled plasma source for the Gaseous electronics conference of rf references cell," *J. Res. Natl. Inst. Stand. Technol.*, vol. 100, pp. 427–439, 1995.
- [39] J. R. Woodworth, P. A. Miller, R. J. Shul, I. C. Abraham, B. P. Aragon, T. W. Hamilton, and C. G. Willison, "Ions in holes: An experimental study of ion distributions inside surface features on radio-frequency-biased wafers in plasma etching discharges," *J. Appl. Phys.*, vol. 92, pp. 716–723, 2002.
- [40] R. J. Shul and S. J. Pearton, *Handbook of Advanced Plasma Processing Techniques*. Berlin, Germany: Springer-Verlag, 2002, p. 148.
- [41] V. A. Godyak, R. B. Piejak, and B. M. Alexandrovich, "A simple analysis of an inductive rf discharge," *Plasma Sources Sci. Technol.*, vol. 1, p. 36, 1992.
- [42] D. N. Ruzic, *Electric Probes for Low Temperature Plasmas*. New York: Amer. Vacuum Soc., 1994.
- [43] J. R. Woodworth, M. E. Riley, D. C. Meister, B. P. Aragon, M. S. Le, and H. H. Sawin, "Ion energy and angular distributions in inductively coupled radio frequency discharges in argon," *J. Appl. Phys.*, vol. 80, pp. 1304–1311, 1996.

**Doosik Kim** received the Ph.D. degree in chemical engineering from the University of Houston, Houston, TX, in 2002. His doctoral research included the modeling and simulation of plasma sheath and glow discharge plasma reactors.



**Demetre J. Economou** received the M.S. and Ph.D. degrees in chemical engineering from the University of Illinois at Urbana-Champaign, IL, in 1983 and 1986, respectively.

Since 1986, he has been with the Chemical Engineering Department at the University of Houston, Houston, TX. His research interests include plasma reactor modeling and simulation, plasma diagnostics, ion-ion plasmas, neutral beam processing, atomic layer etching, plasma-surface interactions, and chemical vapor deposition. He is

the author or coauthor of over 120 papers and book chapters in these areas.

**J. R. Woodworth**, photograph and biography not available at the time of publication.

**P. A. Miller**, photograph and biography not available at the time of publication.

**R. J. Shul**, photograph and biography not available at the time of publication.

**B. P. Aragon**, photograph and biography not available at the time of publication.

**T. W. Hamilton**, photograph and biography not available at the time of publication.

**C. G. Willison**, photograph and biography not available at the time of publication.